ASAXS study of CaF$_2$ nanoparticles embedded in a silicate glass matrix
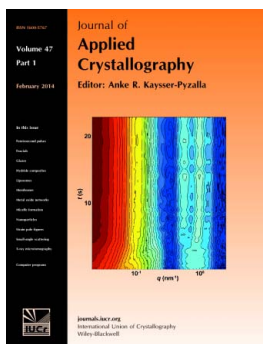
**Armin Hoell, Zoltan Varga, Vikram Singh Raghuwanshi, Michael Krumrey,
Christian Bocker and Christian Rüssel**

Many research topics in condensed matter research, materials science and the life sciences make use of crystallographic methods to study crystalline and non-crystalline matter with neutrons, X-rays and electrons. Articles published in the *Journal of Applied Crystallography* focus on these methods and their use in identifying structural and diffusion-controlled phase transformations, structure-property relationships, structural changes of defects, interfaces and surfaces, *etc.* Developments of instrumentation and crystallographic apparatus, theory and interpretation, numerical analysis and other related subjects are also covered. The journal is the primary place where crystallographic computer program information is published.

Crystallography Journals Online is available from **journals.iucr.org**

ASAXS study of CaF$_2$ nanoparticles embedded in a silicate glass matrix[1]

Armin Hoell,[a]* Zoltan Varga,[b] Vikram Singh Raghuwanshi,[c] Michael Krumrey,[d] Christian Bocker[e] and Christian Rüssel[e]

[a]Helmholtz-Zentrum Berlin für Materialien und Energie, Hahn-Meitner-Platz 1, Berlin, D-14109, Germany, [b]Institute of Molecular Pharmacology, Research Centre for Natural Sciences, Pusztaszeri út 59-67, H-1025, Budapest, Hungary, [c]Humboldt Universität zu Berlin, Insitute für Chemie, Brook-Taylor-Strasse 2, D-12489, Berlin, Germany, [d]Physikalisch-Technische Bundesanstalt (PTB), Abbestrasse 2-12, D-10587, Berlin, Germany, and [e]Otto-Schott-Institut für Glaschemie, Friedrich-Schiller-Universität Jena, Fraunhoferstrasse 6, D-07743, Jena, Germany. Correspondence e-mail: hoell@helmholtz-berlin.de

The formation and growth of nanosized CaF$_2$ crystallites by heat treatment of an oxyfluoride glass of composition 7.65Na$_2$O–7.69K$_2$O–10.58CaO–12.5CaF$_2$–5.77Al$_2$O$_3$–55.8SiO$_2$ (wt%) was investigated using anomalous small-angle X-ray scattering (ASAXS). A recently developed vacuum version of the hybrid pixel detector Pilatus 1M was used for the ASAXS measurements below the Ca K-edge of 4038 eV down to 3800 eV. ASAXS investigation allows the determination of structural parameters such as size and size distribution of nanoparticles and characterizes the spatial distribution of the resonant element, Ca. The method reveals quantitatively that the growing CaF$_2$ crystallites are surrounded by a shell of lower electron density. This depletion shell of growing thickness hinders and finally limits the growth of CaF$_2$ crystallites. Moreover, in samples that were annealed for 10 h and more, additional very small heterogeneities (1.6 nm diameter) were found.

1. Introduction

Polycrystalline and partially crystalline materials are promising candidates as functional optical materials. The crucial prerequisite for their application is full transparency in the interesting wavelength range and hence negligible scattering losses (Edgar *et al.*, 2006; Hendy, 2002). In the case of partially crystalline materials obtained by glass crystallization, transparency can predominantly be achieved by crystals with sizes in the nanometre range and a narrow crystal size distribution. Once nuclei are formed in a glass, they immediately start to grow, and hence, different crystal sizes are formed depending on the nucleation time. As soon as the oversaturation of those components from which the crystals are formed in the glassy phase approaches zero, the crystal sizes and the crystallite size distribution are affected by Ostwald ripening. For a small volume concentration of the particles, the particle size distribution can be estimated according to the Lifshitz–Slyozov–Wagner theory. For higher particle concentrations, the distribution is much broader (Brailsford & Wynblatt, 1979; Lifshitz & Slyozov, 1961; Jayanth & Nash, 1989).

However, even narrower size distributions have recently been reported (Bocker *et al.*, 2009). These size distributions can only be obtained if the crystal growth velocity decreases during the course of the crystallization. This can be achieved by hindered diffusion of the crystal-forming components. This self-limiting process was first observed in oxyfluoride silicate glasses from which BaF$_2$ or CaF$_2$ can be precipitated (Rüssel, 2005; Bocker & Rüssel, 2009). The crystal growth velocity decreases strongly with time and approaches zero. During nucleation and subsequent crystal growth, the glassy phase near the crystals is depleted in fluoride and barium or calcium and hence enriched in silica. This leads to an increase in the local viscosity, resulting in a decrease of the diffusion coefficients (Bocker *et al.*, 2010; Bhattacharyya *et al.*, 2009; de Almeida *et al.*, 2008; Avramov, 2005). Hence, a core–shell structure is formed which acts as a barrier, limiting further crystal growth. A homogeneous dispersion of the crystals in the glassy matrix and a very narrow crystal size distribution are enabled, which lead to ultra-transparent glass ceramics (Bocker *et al.*, 2009; Edgar, 2007). This mechanism has been proven by the increase in viscosity during crystallization (Bocker *et al.*, 2010) and in the case of BaF$_2$ crystallization by transmission electron microscopy (TEM) studies using electron energy-loss spectroscopy (EELS; Bhattacharyya *et al.*, 2009). Here, the formation of a diffusion barrier enriched in SiO$_2$ has been directly observed. Unfortunately, direct observation cannot be easily achieved in oxyfluoride glasses containing CaF$_2$ nanoparticles because of the serious beam

---

damage of the CaF_2 crystals caused by the electron beam itself.

In the case of the silicate glass system SiO_2/Al_2O_3/K_2O/Na_2O/BaF_2/BaO in which a crystallization of BaF_2 takes place, the core–shell structure has also been proven by small-angle X-ray scattering (SAXS) and especially anomalous SAXS (ASAXS) (Raghuwanshi et $al.$, 2012). Here also the effect of heat treatment on size, shape, size distribution and composition of the BaF_2 nanocrystals was studied. SAXS experiments enable the determination of particle sizes in the range from about 1 to 100 nm. The anomalous dispersion near the X-ray absorption edge of an element distributed in the sample helps to determine the phase composition of nanosized clusters (Haas et $al.$, 2010, 2008; Haug et $al.$, 2009; Hoell et $al.$, 2001).

In the present article, we studied nanosized CaF_2 crystals formed during thermal annealing in an SiO_2/Al_2O_3/K_2O/Na_2O/CaF_2/CaO glass. Since microscopic studies were not successful in this system, SAXS (Glatter & Kratky, 1982; Feigin & Svergun, 1987; Guinier & Fournet, 1955) and ASAXS were used to determine the nanostructure, the spatial arrangement and the concentration of calcium in the nanoparticles and in a surrounding layer as well as the matrix. We performed ASAXS experiments at X-rays energies near the Ca K absorption edge. The present work provides direct evidence of the formation of CaF_2 particles surrounded by an SiO_2-enriched layer simulated as a core–shell model based on the ASAXS technique.

2. Theory

SAXS is the method of choice for the structural characterization of nano-objects in the size range from about 1 to 100 nm. SAXS is capable of determining the sizes and size distributions of the nanoparticles (NPs). However, in the case of a multi-component system, the small-angle scattering of the matrix is also added to the scattering from the NPs, which makes the data evaluation challenging. Separation of the scattering contributions of the different constituents of this complex system can be achieved by using ASAXS, which is based on the energy dependence of the atomic scattering factor of the elements. Far from the absorption edges the atomic scattering factor is equal to the number of electrons of the given element, but it shows strong variation in the vicinity of an absorption edge. In general, the atomic scattering factor, $f(E)$, can be written as

$$f(E) = f_o + f'(E) + if''(E), \qquad (1)$$

where $f_o + f'(E)$ and $f''(E)$ are the real and the imaginary parts of the atomic scattering factors. The anomalous dispersion corrections, $f'(E)$ and $f''(E)$, carry information about the energy dependency of the contrast of a given element, which plays an important role at X-ray energies near an absorption edge. The dispersion corrections $f'(E)$ and $f''(E)$ are related to each other by the well known Kramers–Kronig relation. The total scattering intensity, $I(q, E)$, is a function of the X-ray energy and of the magnitude of the momentum transfer $q = (4\pi/\lambda)\sin(\theta/2)$, where λ is the X-ray wavelength and θ is the

scattering angle. It can be written with the anomalous contributions as

$$I(q, E) = f_o^2 I_0(q) + 2f_o f'(E) I_{0R}(q) + \left[f'(E)^2 + f''(E)^2 \right] I_R(q). \qquad (2)$$

This equation consists of three parts. The energy-independent normal SAXS term $I_0(q)$, the scattering cross term $I_{0R}(q)$ and the pure resonant scattering, $I_R(q)$ (Stuhrmann, 1985). The form of equation (2) implies that scattering measurements must be performed on at least three different energies near but below the absorption edge of the resonant element, and this allows the separation of the resonant scattering term, $I_R(q)$. This resonant scattering term contains information about the spatial distribution of the resonant chemical element distributed in nanosized structures only (Hoell et $al.$, 2009).

The scattering intensity for non-interacting particles with a number distribution $N(r)$ can be calculated by the following expression:

$$I(q) = \int_0^\infty N(r) |V_p(r) F(q, r, \Delta\eta)|^2 dr + Bg, \qquad (3)$$

where $F(q, r, \Delta\eta)$ is the scattering amplitude determined by the shape and size of the particles and the term Bg describes a background that is caused by the fluctuation scattering (density and composition) from fluorescence and from resonant Raman scattering. The volume of the particle is given by $V_p(r)$. The form factor, F^2, for a homogenous sphere with radius r is defined as follows:

$$F_{sphere}^2(q, r, \Delta\eta) = \left[\Delta\eta \, 3 \frac{\sin(qr) - (qr)\cos(qr)}{(qr)^3} \right]^2, \qquad (4)$$

where $\Delta\eta$ is the electron density difference between the particle and the matrix. Similarly, the scattering amplitude, F, for a spherical core–shell model is defined as:

$$F_{sphere\,shell}(q, r_t, \Delta\eta_s, v, \mu) = F_{sphere}(q, r_t, \Delta\eta_s) - F_{sphere}[q, vr_t, \Delta\eta_s(1 - \mu)], \qquad (5)$$

where $\Delta\eta_s = \eta_{shell} - \eta_{matrix}$ is the electron density difference between the shell and the matrix and $v\Delta\eta_s$ is the electron density difference between the core and the matrix relative to the shell, r_t is the total radius of the particles, and $r = vr_t$ ($0 < v < 1$) is the radius of the core. The scattering density is evaluated as the product of the atom number density and the number of electrons in each atom.

3. Experimental and fitting procedure

Glasses with the composition 7.65Na_2O–7.69K_2O–10.58CaO–12.5CaF_2–5.77Al_2O_3–55.8SiO_2 (wt%) were melted from reagent grade Na_2CO_3, K_2CO_3, $CaCO_3$, CaF_2, $Al(OH)_3$ and SiO_2 (quartz) in batches of 200 g in a covered platinum crucible at 1753 K. The melts were subsequently cast on a copper block and placed in a furnace preheated to 823 K. The furnace was then switched off and the samples were allowed to

cool. The samples were thermally treated at a temperature of 823 K for different annealing times up to 160 h in a muffle furnace. The as-prepared glasses and thermally treated samples were cut into $6 \times 6 \times 15$ mm pieces. X-ray diffraction (XRD) patterns of the samples were recorded using a Siemens D5000 diffractometer. The density of the as-prepared glass was measured to be 2.5990 Mg m^{-3}. The density of the glass ceramic is 2.6155 Mg m^{-3} after 80 h annealing at 823 K.

ASAXS measurements were performed at the BESSY II synchrotron radiation facility (HZB, Berlin, Germany) using the four-crystal monochromator (FCM) beamline of the Physikalisch-Technische Bundesanstalt (PTB), the German National Metrology Institute (Krumrey & Ulm, 2001). The combination of this beamline and the ASAXS instrument of the HZB (Hoell *et al.*, 2007) has already been described (Gleber *et al.*, 2010). The scattering patterns were recorded with a new in-vacuum large-area hybrid pixel detector (Pilatus 1M, Dectris Ltd, Switzerland). As no window is required between the sample and the sensitive modules of this detector, the entire photon energy range of the FCM beamline from 1.75 to 10 keV can be used for SAXS and ASAXS measurements. The quantum efficiency of this detector at the Ca K-edge is about 85% (Donath *et al.*, 2013), while that of a previously used gas delay-line detector is below 2% owing to the finite transmission of the required vacuum window. The incoming photon flux was permanently measured with a thin photodiode operated in transmission mode (Krumrey *et al.*, 2007).

ASAXS measurements were performed at five different energies (see Table 1 and Fig. 1) below but close to the Ca K-edge at 4038 eV. The collected two-dimensional raw scattering data patterns were corrected for possible variations in the incoming photon flux, sample transmission, scattering background and geometrical effects by spherical projection. The scattering background arising from beamline components was measured before each sample sequence using an empty sample holder. The sample transmissions were measured
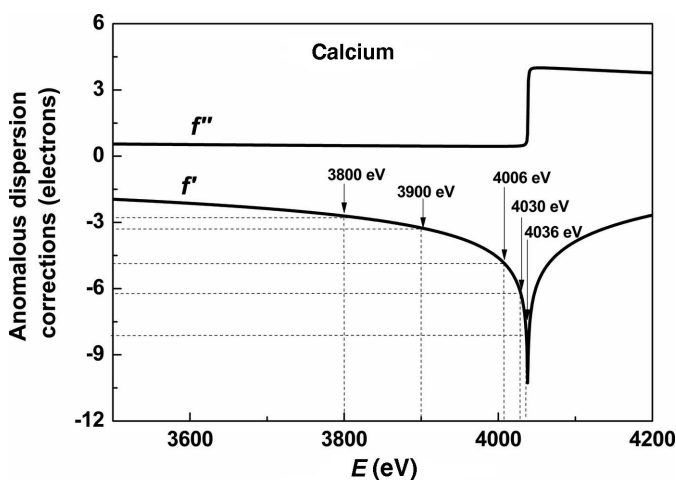

Figure 1
Anomalous dispersion corrections f' and f'' for Ca near the Ca K-edge (4038 eV). The five X-ray energies for the ASAXS measurements are indicated.

Table 1
Energy-dependent parts of the atomic scattering factor, f' and f'', of calcium near the Ca K-edge at 4038 eV for the five X-ray energies used for ASAXS measurements.

Data taken from Cromer & Liberman (1970) under consideration of the chemical shift ($\Delta E = E - 4038$ eV).

	E (eV)	ΔE (eV)	f'	f''
E_1	3800	−238	−2.708	0.478
E_2	3900	−138	−3.247	0.457
E_3	4006	−32	−4.795	0.445
E_4	4030	−8	−6.338	0.475
E_5	4036	−2	−7.874	0.582

directly before each scattering measurement by placing a windowless silicon photodiode behind the sample into the beam path. In order to have direct control of statistical errors and to take care of possible time-dependent variations of beam conditions, the measurements were separated into several short runs and then averaged. Finally, the scattering intensity has been converted to the differential cross section per unit volume by using a calibrated glassy carbon standard of 90 µm thickness that was measured at the beginning of each sample sequence. The axis of the momentum transfer q was calibrated by the known d spacing of a silver behenate sample (Binnemans *et al.*, 2004).

To calculate resonant scattering curves, $I_R(q)$, according to equation (2), the anomalous dispersion corrections f' and f'' are taken from the quantum mechanical calculations for free atoms made by Cromer & Liberman (1970). XANES measurements were performed at the Ca K absorption edge. A chemical shift of +5 eV was found for all samples. This shift was taken into account and all energies were corrected accordingly. As an Si(111) four-crystal monochromator with a resolving power of about 10^4 was used (Krumrey & Ulm, 2001), an energy smearing of the f' and f'' values could be neglected. The highest X-ray energy was 2 eV below the edge.

The software *SASfit* (http://kur.web.psi.ch/sans1/SANSSoft/sasfit.html), which basically provides nonlinear least-squares fitting of equation (3) for different structural models, was used to obtain the average radius of the nanostructures, the shell thickness and the relative experimental contrasts. *SASfit* requires a predefined shape of the size distribution. The scattering contrasts, the particle size distribution parameters and the number of particles are fit parameters.

In the present investigation it turned out that for fitting the SAXS curves a spherical core–shell model combined with a sphere model has to be used. The total scattering intensity can be modelled by the superposition of two size distributions of spherical core–shell structures and of spheres and can be calculated according to

$$I_{\text{SAXS}}(q) = \int_0^\infty N(r_t) \left| V_p(r_t) F_{\text{sphere shell}}(q, r_t, \Delta\eta_s, v, \mu) \right|^2 dr$$
$$+ \int_0^\infty N(r) \left| V_p(r) F_{\text{sphere}}(q, r, \Delta\eta) \right|^2 dr + \text{Bg}. \quad (6)$$

The two-sphere model had also to be used to fit the resonant scattering curves, $I_R(q)$, as calculated from equation (2). The resonant scattering intensity resulting from larger spherical particles with an average radius r_1 and smaller spherical particles with an average radius r_2 is given as

$$I_{\text{resonant}}(q) = \int\limits_0^\infty N(r_1)\left|V_p(r_1)\,F_{\text{sphere}}(q, r_1, \Delta\eta)\right|^2 \mathrm{d}r$$
$$+ \int\limits_0^\infty N(r_2)\left|V_p(r_2)\,F_{\text{sphere}}(q, r_2, \Delta\eta)\right|^2 \mathrm{d}r + \text{Bg}. \quad (7)$$

4. Results and discussion

The as-prepared glass and the three annealed samples (annealed at 823 K for between 4 and 40 h) are visually transparent. Fig. 2 shows the XRD patterns of all four samples measured as described by Rüssel (2005) and Bocker & Rüssel (2009). The as-prepared sample shows no Bragg peaks. After thermal treatment, Bragg peaks appear at three angles (28.3, 47 and 56°) and can be attributed to crystalline CaF_2 (JCPDS 35-0816). All the peaks are significantly broadened. The width of the Bragg peaks does not change on increasing the annealing time from 4 to 40 h, but their intensity increases with annealing time.

The size, size distribution, volume fraction and shape of the particles in the glass matrix can be obtained from the SAXS measurements, while the composition fluctuations and the shell thickness were determined from the ASAXS curves. The SAXS curves measured at 3800 eV, thus far from the edge, are shown in Fig. 3 for all four samples. Obviously, all samples show pronounced small-angle scattering, identifying that nanostructures already occur in the as-prepared glass. The shape of the scattering curves is similar for the as-prepared and the 4 h annealed samples, while it differs for the prolonged annealed samples (10 and 40 h). The two longer annealed samples have also a similar shape. The as-prepared and the 4 h annealed samples show small shoulders at about $q = 0.7$ nm^{-1} and a steep slope at small q values, while the two longer annealed samples show two pronounced shoulders. The steep slopes proportional to q^{-4} for all scattering curves at the smallest q values ($q < 0.07$ nm^{-1}) are caused by large additional structures in the size range above 100 nm as confirmed
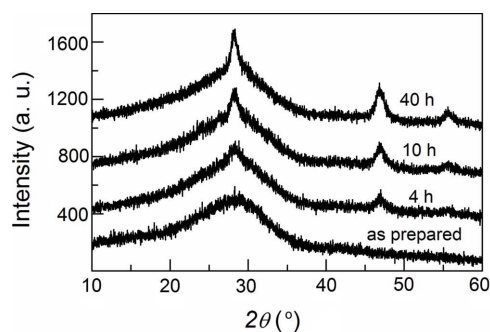
Table 2
Main structural sizes parameters for all four samples derived by fitting the ASAXS curves as well as the resonant curves for both longer annealed samples.

The numbers in parentheses are standard uncertainties on the least significant digit.

Sample at 823 K	Particle 1 radius (nm)	Shell thickness (nm)	Particle 2 radius (nm)	Resonant curve particle 1 (nm)	Resonant curve particle 2 (nm)
Unannealed	2.0 (3)	0.4 (1)	–	–	–
4 h	2.4 (3)	0.4 (1)	–	–	–
10 h	12.4 (5)	0.7 (2)	0.8 (2)	12.2 (5)	0.7 (2)
40 h	12.6 (5)	1.2 (2)	0.8 (2)	12.4 (5)	0.8 (2)

by the structure modelling procedure. These structures are additional heterogeneities and their total structural information is in the q range below $q = 0.05$ nm^{-1}, which is beyond the instrumental resolution.

A slight shoulder between 0.5 and 1 nm^{-1} is the first hint of small nanosized particles that can occur in the as-prepared and 4 h annealed samples. The structure modelling procedure reveals that small particles are formed with radii of 2.0 and 2.4 nm, respectively, surrounded by a shell (Table 2). Other possible structure models also with narrow size distributions could be excluded in the course of structure modelling. The shape of the scattering curves is significantly changed for 10 and 40 h annealing with respect to the 4 h annealed sample. Additionally, a pronounced shoulder appears at about $q = 0.15$ nm^{-1} with one order of magnitude higher intensity. The differential scattering cross section is larger for the 40 h annealed sample, while the shape of the scattering curve is similar to the 10 h annealed sample, taking into account the contribution from the angle-independent scattering constant, the so-called fluctuation scattering term. This proves that the nanostructure remains almost unchanged, but the particle number density increases with increasing annealing time from 10 to 40 h.

Figs. 4 and 5 show the ASAXS measurements at five X-ray energies below the Ca absorption edge for the samples
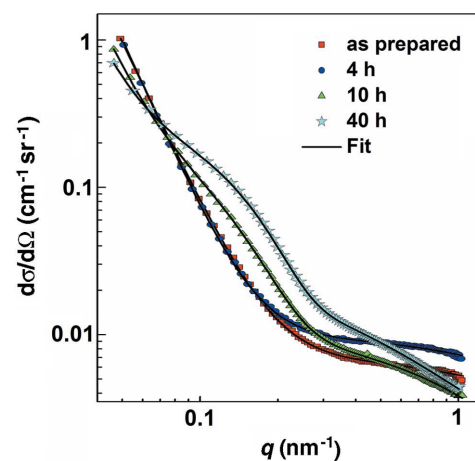
Figure 2
XRD patterns of samples with different annealing times at 823 K. The peaks identify the formation of CaF_2 crystallites.

Figure 3
SAXS curves of glasses after different annealing times at 823 K, measured at an X-ray energy of 3800 eV.

annealed for 10 and 40 h. In both cases we observe a similar and strong variation of $d\sigma/d\Omega$ with the X-ray energy. The scattering curves of these two samples obtained far below the Ca K-edge at 3800 eV show two significant shoulders. With increasing energy towards the Ca absorption edge, these two shoulders almost vanish and the total scattering intensity decreases. At the energy near the Ca K-edge (4036 eV), featureless scattering curves remain. The slope of q^{-4} for the scattering curves at $q < 0.05$ nm^{-1} remains unchanged and energy independent during the contrast variation. The influence of the resonant Raman scattering can be observed at large q values for the X-ray energies of 4030 and 4036 eV by an additional increasing q-independent scattering contribution.

It turned out that the two distinct shoulders of the scattering curves in Figs. 4 and 5 cannot be explained by any unimodal size distribution, narrow or broad, of spherical crystals. A core–shell structure and bimodal distributions of particles have therefore been considered.
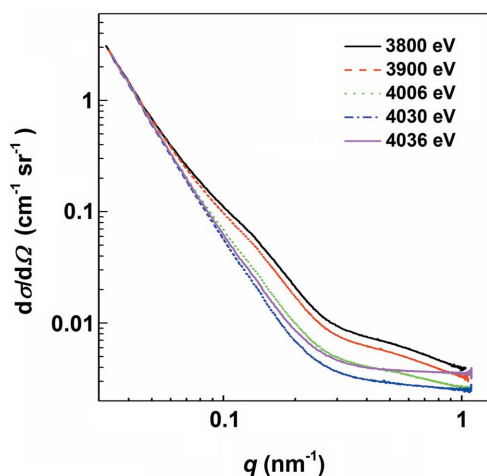

Figure 4
ASAXS curves of the glass ceramic annealed at 823 K for 10 h, showing a strong energy dependence of their shape arising from the spatial distribution of the Ca atoms on the nanometre scale. The X-ray energies are corrected by the chemical shift of the samples of +5 eV.
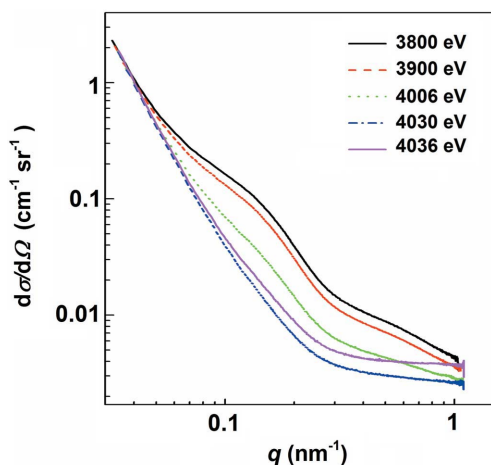

Figure 5
ASAXS curves of the glass sample annealed at 823 K for 40 h. The energy-dependent effect is similar but more pronounced than in Fig. 4.

Furthermore, the pure resonant scattering curves, $I_R(q)$, which contain the spatial distribution of the Ca atoms were calculated for the samples annealed for 10 and 40 h by solving the linear equation system (2) from three scattering curves measured at three different energies close to the Ca K absorption edge (Stuhrmann, 1985). While measurements were performed at five different energies, different combinations of energies were used to average the resulting resonant scattering curves. The two resulting resonant scattering curves for 10 and 40 h annealing are shown in Fig. 6. The two scattering curves are similar in shape and show two shoulders. They are more pronounced than the observed two shoulders already described for the total small-angle scattering in Figs. 4 and 5.

Regarding the analysis of the nanostructure, the program *SASfit* was used for all four samples and for the resonant scattering curves. It turned out that a lognormal size distribution of particles fits the scattering curves well. While fitting a particular SAXS curve, all the structure determining parameters, size distribution parameters and contrasts of the particles are free variables. Attempts were made to fit the curves by three structure models: (i) spheres, (ii) spherical core–shell structures, and (iii) a combination of two independent size distributions of spheres and core–shell structures with different electron densities. As already discussed for the scattering curves of the longer annealed samples, no unimodal size distribution of spherical particles is suited to fit the scattering curves, which provides hints for the presence of some other particles or shell-like regions around the particles. The scattering curves can be modelled assuming core–shell-like structures and, for longer annealing times, a contribution from additional very small particles.

The averaged structural size parameters for all samples as calculated from the total scattering and the resonant scattering curves of the Ca atoms for the two longer annealed samples are given in Table 2. Core–shell particles occur in the as-prepared sample and in the annealed glass ceramics. The existence of particles in the as-prepared state is already a new
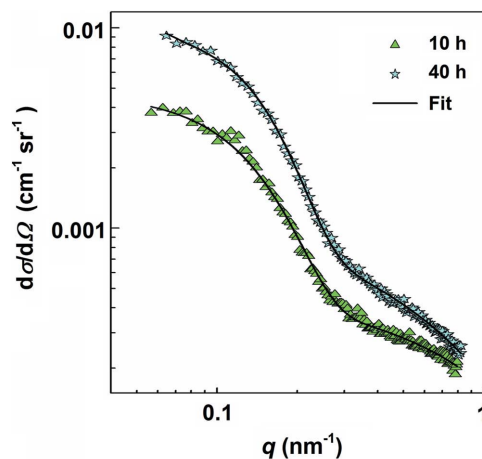

Figure 6
Pure resonant scattering curves for Ca as calculated by the method from Stuhrmann (1985) for 10 and 40 h annealing (symbols). The lines show the fits with the structural model.

result that could not be derived from the XRD measurements (Fig. 2) and the TEM investigations. ASAXS reveals a slight growth of the particles until about 4 h annealing. After that, the size increases by a factor of five until 10 h annealing, while the further growth of the particles (core region) almost stops after this time. Even after this growth stop of the CaF_2 crystals, the shell thickness continued to grow. Moreover, a secondary type of rather small spherical heterogeneities was found for longer annealing times by ASAXS (Table 2). In the case of these small heterogeneities (about 1.6 nm diameter) no additional shell region was identified.

The structural analysis of the two resonant scattering curves in Fig. 6 which are caused by the spatial distribution of the Ca atoms in the samples reveal the existence of two kinds of particles with almost the same sizes as calculated from the total scattering curves (Figs. 4 and 5, Table 2). The major difference from the total scattering is that the larger particles have no shell, but the particle sizes are identical. This finding is important and means that the electron density contrast causing a small-angle scattering effect between the shell and the matrix with respect to the concentration of the Ca atoms can be neglected. Therefore, the dominating contrast in the case of the resonant curves is between the particles and the shell region. The larger particles with radii of about 12.5 nm are the CaF_2 nanocrystals (in accordance with XRD; Rüssel, 2005). The smaller heterogeneities with radii of about 0.8 nm (Table 2) have a contrast to the remaining glass matrix, but it is not evident if their Ca concentration is higher or lower.

The volume-weighted particle size distributions are shown in Fig. 7, as calculated from the structural fit for the resonant scattering after 40 h annealing. These particle size distributions are similar to those after 10 h annealing. The size distribution of the larger particles is relatively small and not extended towards higher radii. This gives further evidence pointing to a hindered or self-limiting growth process.

Fig. 8 shows the relative radial averaged electron density profile of the larger particles (CaF_2 nanocrystals) derived for two different X-ray energies with respect to the remaining glass matrix for the sample annealed at 823 K for 40 h. The

particles have the highest electron density and the shell region has the lowest. Thus it is depleted of the elements and structural groups with high electron densities, e.g. Ca atoms. When the X-ray energy of the SAXS measurement is increased from 3800 to 4036 eV, the electron density profile shows changes caused by the anomalous scattering behaviour of the Ca atoms (Fig. 1). As only the 'effective electron density' of the Ca atoms decreases, this implies that the shell region is depleted of Ca and also contains fewer Ca atoms and/or a lower mass density than the matrix.

The influence of the annealing time on the relative radial averaged electron density profile of the larger core–shell particles (CaF_2) is shown at an X-ray energy of 3800 eV in Fig. 9. The relative contrasts are calculated and normalized as in Fig. 8. The shell has a low electron density and its thickness

Figure 8
Relative radially averaged electron densities with respect to the glass matrix for the large CaF_2 crystals after 40 h annealing at energies of 3800 and 4036 eV. ASAXS reveals a shell region with a lower electron density than the matrix. The relative electron density change with increasing X-ray energy (red) indicates that some Ca remains in the shell region.
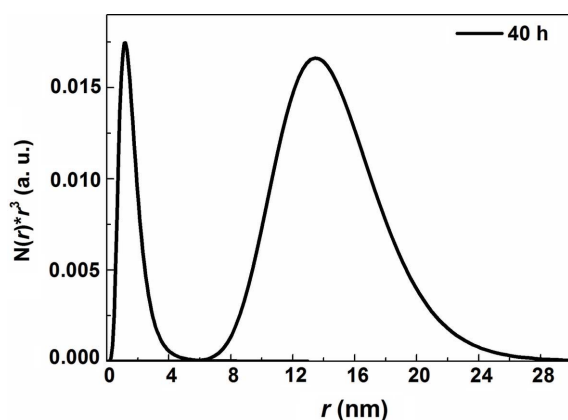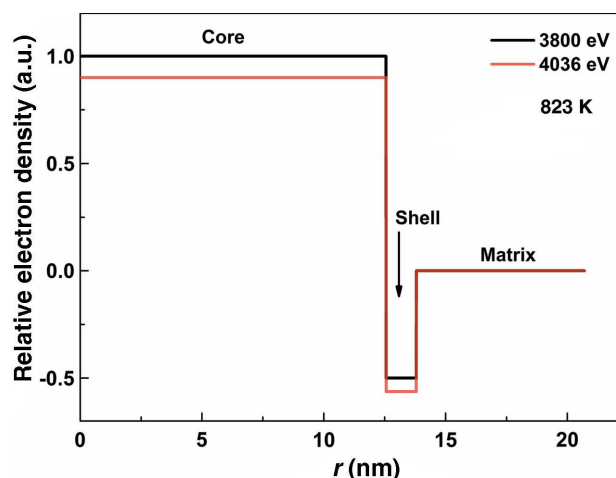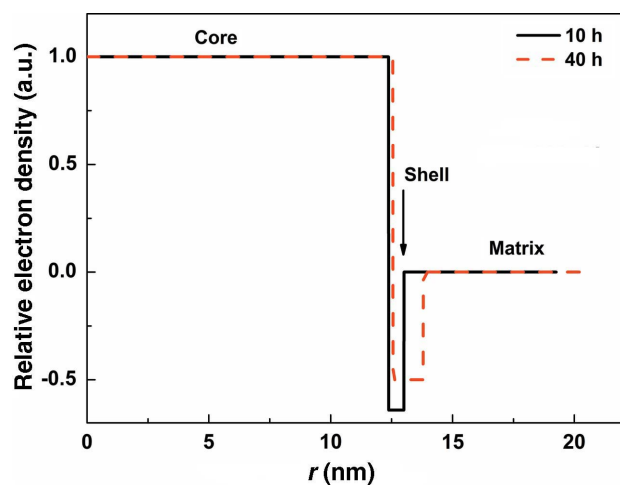

Figure 7
Volume-weighted particle size distributions of the two kinds of particles, crystals and small heterogeneities, for 40 h annealing as calculated from the resonant curve. For the CaF_2 crystals the core radius is shown.

Figure 9
Development of the relative radially averaged electron density with respect to the glass matrix for the large CaF_2 crystals at an energy of 3800 eV. The shell region grows while its concentration difference with respect to the matrix decreases.

increases from 0.7 to 1.2 nm while the particle size remains almost constant. Moreover, the electron density contrast between the shell region and the glass matrix decreases. This is an important result. The crystal growth is already limited after 10 h annealing at 823 K. The shell is only 0.7 nm thick and has a low electron density. The electron density increases during further annealing so that the contrast to the glass decreases. That indicates a diffusion-controlled element exchange between the shell and the matrix, reducing the concentration gradient while the shell thickness grows. A similar behaviour was observed for an Al-rich diffusion barrier in a glass containing $ZrTiO_4$ nanocrystals using high-resolution TEM in combination with EELS (Höche et al., 2012).

The density of the CaF_2 crystallites is 3.18 Mg m^{-3} and the glass ceramics densities vary between 2.599 and 2.615 Mg m^{-3}. A pure SiO_2 glass would have a density of about 2.2 Mg m^{-3}. Therefore, the shell region can have only a lower electron density in comparison to the matrix (as confirmed in Figs. 8 and 9) if the shell is depleted of Ca atoms and of other oxides so that finally the concentration of SiO_2 is increased in the shell region with respect to the glass matrix. This model can explain the lower electron density in the shell-like region surrounding the CaF_2 crystallites. A similar result was obtained when BaF_2 crystallizes in an oxyfluoride glass (Raghuwanshi et al., 2012). This depletion zone enriched by SiO_2 is also in agreement with the results reported by Rüssel (2005) and de Almeida et al. (2008) who found a decrease in T_g and an increase of the glass viscosity during the crystallization process of CaF_2.

ASAXS revealed the formation of a secondary type of small spherical particle after long annealing times. No quantitative results for the composition of the shell region is possible like in case of BaF_2, because the spherical particles also change the remaining matrix composition. The system of equations for the compositions of the two particle types and the remaining glass matrix is thus underdetermined.

5. Conclusions

Crystalline CaF_2 was precipitated from a glass of composition 7.65Na$_2$O–7.69K$_2$O–10.58CaO–12.5CaF$_2$–5.77Al$_2$O$_3$–55.8SiO$_2$ (wt%). This glass could have interesting nonlinear optical applications if it were to be doped with rare earth elements by exhibiting up and down conversion of optical light.

It was known from former studies that nanosized CaF_2 crystallites are precipitated (XRD) during annealing at 823 K. XRD has shown a growth stop after a certain annealing time, which is accompanied by an increase of the glass viscosity and a decrease in T_g. Therefore, ASAXS was used to give quantitative evidence of the existence and size of a shell surrounding the growing crystallites that results in the observed hindered growth and finally a growth cessation. The crystallites stop growing after about 10 h annealing at 823 K and reach a diameter of about 25 nm. They are surrounded by a shell with a low electron density. That can be explained by a depletion of the shell region and an enrichment of SiO_2. Whereas the size growth stops, the volume fraction of the

crystallites continues to increase and the shell diameter grows while a diffusion-controlled element exchange between shell and matrix reduces the concentration gradient. Already the as-prepared sample contains particles with diameters of about 4 nm. Additional very small heterogeneities are found after long annealing with diameters of about 1.6 nm.

References

Almeida, R. P. F. de, Bocker, C. & Rüssel, C. (2008). Chem. Mater. 20, 5916–5921.

Avramov, I. (2005). J. Non-Cryst. Solids, 351, 3163–3173.

Bhattacharyya, S., Bocker, C., Heil, T., Jinschek, J. R., Höche, T., Rüssel, C. & Kohl, H. (2009). Nano Lett. 9, 2493–2496.

Binnemans, K., Van Deun, R., Thijs, B., Vanwelkenhuysen, I. & Geuens, I. (2004). Chem. Mater. 16, 2021–2027.

Bocker, C., Avramov, I. & Rüssel, C. (2010). Chem. Phys. 369, 96–100.

Bocker, C., Bhattacharyya, S., Höche, T. & Rüssel, C. (2009). Acta Mater. 57, 5956–5963.

Bocker, C. & Rüssel, C. (2009). J. Eur. Ceram. Soc. 29, 1221–1225.

Brailsford, A. & Wynblatt, P. (1979). Acta Metall. 27, 489–497.

Cromer, D. T. & Liberman, D. (1970). J. Chem. Phys. 53, 1891–1898.

Donath, T., Brandstetter, S., Cibik, L., Commichau, S., Hofer, P., Krumrey, M., Lüthi, B., Marggraf, S., Müller, P., Schneebeli, M., Schulze-Briese, C. & Wernecke, J. (2013). J. Phys. Conf. Ser. 425, 062001.

Edgar, A. (2007). J. Mater. Sci. Mater. Electron. 18, 335–338.

Edgar, A., Williams, G. & Hamelin, J. (2006). Curr. Appl. Phys. 6, 355–358.

Feigin, L. A. & Svergun, D. I. (1987). Structure Analysis by Small-Angle X-ray and Neutron Scattering. New York: Plenum Press.

Glatter, O. & Kratky, O. (1982). Small-Angle X-ray Scattering. New York: Academic Press.

Gleber, G., Cibik, L., Haas, S., Hoell, A., Müller, P. & Krumrey, M. (2010). J. Phys. Conf. Ser. 247, 012027.

Guinier, A. & Fournet, G. (1955). Small-Angle Scattering of X-rays. New York: Wiley.

Haas, S., Hoell, A., Wurth, R., Rüssel, C., Boesecke, P. & Vainio, U. (2010). Phys. Rev. B, 81, 184207.

Haas, S., Hoell, A., Zehl, G., Dorbandt, I., Bogdanoff, P. & Fiechter, S. (2008). ECS Trans. 6, 127–138.

Haug, J., Kruth, H., Dubiel, M., Hofmeister, H., Haas, S., Tatchev, D. & Hoell, A. (2009). Nanotechnology, 20, 505705.

Hendy, S. (2002). Appl. Phys. Lett. 81, 1171.

Höche, T., Patzig, C., Gemming, T., Wurth, R., Rüssel, C. & Avramov, I. (2012). Cryst. Growth Des. 12, 1556–1563.

Hoell, A., Bley, F., Wiedenmann, A., Simon, J., Mazuelas, A. & Boesecke, P. (2001). Scr. Mater. 44, 2335–2339.

Hoell, A., Tatchev, D., Haas, S., Haug, J. & Boesecke, P. (2009). J. Appl. Cryst. 42, 323–325.

Hoell, A., Zizak, I., Bieder, H. & Mokrani, L. (2007). German Patent No. DE102006029449.

Jayanth, C. S. & Nash, P. (1989). J. Mater. Sci. 24, 3041–3052.

Krumrey, M., Gerlach, M., Hoffmann, M. & Müller, P. (2007). AIP Conf. Proc. 879, 1145–1147.

Krumrey, M. & Ulm, G. (2001). Nucl. Instrum. Methods Phys. Res. Sect. A, 467–468, 1175–1178.

Lifshitz, I. & Slyozov, V. (1961). J. Phys. Chem. Solids, 19, 35–50.

Raghuwanshi, V. S., Hoell, A., Bocker, C. & Rüssel, C. (2012). CrystEngComm, 14, 5215.

Rüssel, C. (2005). Chem. Mater. 17, 5843–5847.

Stuhrmann, H. B. (1985). Resonance Scattering in Macromolecular Structure Research, Advances in Polymer Science, Vol. 67, edited by H. Kausch & H. Zachmann, pp. 123–163. Berlin: Springer-Verlag.